

## EDGE ARTICLE

[View Article Online](#)  
[View Journal](#) | [View Issue](#)Cite this: *Chem. Sci.*, 2015, **6**, 4993

## An efficiently tuned d-orbital occupation of $\text{IrO}_2$ by doping with Cu for enhancing the oxygen evolution reaction activity<sup>†</sup>

Wei Sun,<sup>a</sup> Ya Song,<sup>b</sup> Xue-Qing Gong,<sup>\*b</sup> Li-mei Cao<sup>a</sup> and Ji Yang<sup>\*a</sup>

The oxygen evolution reaction (OER) has been regarded as a key half reaction for energy conversion technologies and requires high energy to create  $\text{O}=\text{O}$  bonds. Transition metal oxides (TMOs) seem to be a promising and appealing solution to the challenge because of the diversity of their d-orbital states. We chose  $\text{IrO}_2$  as a model because it is universally accepted as a current state-of-the-art OER catalyst. In this study, copper-doped  $\text{IrO}_2$ , particularly  $\text{Cu}_{0.3}\text{Ir}_{0.7}\text{O}_\delta$ , is shown to significantly improve the OER activity in acidic, neutral and basic solutions compared to un-doped  $\text{IrO}_2$ . The substituted amount of Cu in  $\text{IrO}_2$  has a limit described by the  $\text{Cu}_{0.3}\text{Ir}_{0.7}\text{O}_\delta$  composition. We determined that the performance of  $\text{Cu}_{0.3}\text{Ir}_{0.7}\text{O}_\delta$  is due primarily to an increase in the Jahn–Teller effect in the  $\text{CuO}_6$  octahedra, and partially to oxygen defects in the lattice induced by the  $\text{IrO}_6$  octahedral geometric structure distortions, which enhance the lift degeneracy of the  $t_{2g}$  and  $e_g$  orbitals, making the  $d_z^2$  orbital partially occupied. This phenomenon efficiently reduces the difference between  $\Delta G_2$  and  $\Delta G_3$  in the free energy from the density functional theoretical (DFT) calculations and can yield a lower theoretical overpotential comparable to that of  $\text{IrO}_2$ . The proposed method of doping with foreign elements to tune the electron occupation between the  $t_{2g}$  and  $e_g$  orbital states of Ir creates an opportunity for designing effective OER catalysts using the TMO groups.

Received 8th April 2015  
Accepted 12th June 2015

DOI: 10.1039/c5sc01251a  
[www.rsc.org/chemicalscience](http://www.rsc.org/chemicalscience)

### Introduction

The oxygen evolution reaction (OER) at the anode is the key half reaction for splitting water into  $\text{H}_2$  fuel and reducing the  $\text{CO}_2$  concentration in fuels (*e.g.*,  $\text{CO}$ ,  $\text{CH}_4$ ) and metal–air batteries.<sup>1–4</sup> However, the OER is a complex process associated with  $4\text{e}/4\text{H}^+$  loss and  $\text{O}=\text{O}$  bond formation, which requires a high overpotential relative to the standard reaction potential ( $E = 1.229$  V,  $\text{pH} = 0$ ) to achieve the desired current density.<sup>1,5,6</sup> The critical step to address the challenge is to find efficient catalysts. One of the most promising catalysts is a transition metal oxide (TMO); this group has nearly infinitely variable properties of its d-orbital states ( $d^0 \sim d^{10}$ ),<sup>7,8</sup> particularly  $t_{2g}$  and  $e_g$ , which can be

systematically modified to optimize the catalytic activity at the surface.<sup>9–11</sup> The OER catalytic activity of TMOs is governed completely by its d-orbital electron structure<sup>12</sup> because the bond making or breaking in the OER processes are based on the O-2p of intermediates bonding with the M-nd of surface sites. Many approaches are being engineered to enhance the OER catalytic activity by doping foreign elements into the host structure or modifying the substitute to increase the number of catalytically active sites.<sup>13–18</sup> Numerous studies show that introducing F,<sup>19</sup> Ru,<sup>20,21</sup> Ta<sup>22</sup> and Zn<sup>23</sup> into  $\text{IrO}_2$  can obtain an improvement in the OER activity. However, there are still important aspects regarding how the doped foreign metals tune the d orbital electronic structure of the host element and further affect its OER activity.

Here, we show that copper (Cu)-doped  $\text{IrO}_2$ , particularly in the  $\text{Cu}_{0.3}\text{Ir}_{0.7}\text{O}_\delta$  composition, exhibits a high OER activity in acidic, neutral and basic solutions ( $\text{pH} \sim 1, 7$  and 13, respectively). We chose  $\text{IrO}_2$  as a model because it has been universally accepted as a current state-of-the-art OER catalyst and maintains a stable structure in water oxidation over a broad pH range.<sup>24–27</sup> The copper is taken as the dopant due to its special electronic structure ( $3\text{d}^{10}4\text{s}^1$ ), and  $\text{Cu}^{2+}$  is widely applied in superconductors.<sup>28–30</sup> In this study, the Cu that is introduced into the  $\text{IrO}_2$  lattice changes the  $\text{IrO}_2$  lattice parameters and further affects the d-orbital distributions of the Ir-5d electrons; these mechanisms are discussed in detail. We also attribute the

<sup>a</sup>State Environmental Protection Key Laboratory of Environmental Risk Assessment and Control on Chemical Processes, School of Resources and Environmental Engineering, East China University of Science and Technology, 130 Meilong Road, Shanghai 200237, P. R. China. E-mail: [yangji@ecust.edu.cn](mailto:yangji@ecust.edu.cn)

<sup>b</sup>Key Laboratory for Advanced Materials, Center for Computational Chemistry and Research Institute of Industrial Catalysis, East China University of Science and Technology, 130 Meilong Road, Shanghai 200237, P. R. China. E-mail: [xgong@ecust.edu.cn](mailto:xgong@ecust.edu.cn)

<sup>†</sup> Electronic supplementary information (ESI) available: Materials, experimental procedures and theoretical calculations; figures including SEM, TEM images, EDS data, EXAFS and XPS spectra, CVs for RHE calibration and polarization curves for mixture of  $\text{CuO}$  and  $\text{IrO}_2$ ; and tables for EDS and comparison of OER activity. See DOI: [10.1039/c5sc01251a](https://doi.org/10.1039/c5sc01251a)



high performance observed to the fact that the doped Cu changes the Ir site electron structure and lifts its  $e_g$  orbital resulting in partial occupation of its  $d_z^2$  orbital.

## Results and discussion

$\text{Cu}_x\text{Ir}_{1-x}\text{O}_\delta$ , with varying compositions, was synthesized hydrothermally *via* doping different amounts of Cu into the  $\text{IrO}_2$  lattice, and allowing crystallization at 600 °C (detailed synthesis information is shown in the ESI†).

Fig. 1a shows the electrochemical characterization of the  $\text{Cu}_{0.3}\text{Ir}_{0.7}\text{O}_\delta$  composition,<sup>31</sup> which exhibited an excellent OER activity in three solutions with different pH values. The  $\eta$  requirements at  $j = 10 \text{ mA cm}^{-2}$ , which is a meaningful reference due to its relevance to solar synthesis,<sup>32</sup> were remarkably small at 351 mV in the acidic solution, 623 mV in the neutral solution and 415 mV in the basic solution, which indicated the excellent performance of  $\text{Cu}_{0.3}\text{Ir}_{0.7}\text{O}_\delta$  in the acidic and neutral solutions; the values were much smaller compared to some reported for effective Co-based catalysts.<sup>33–35</sup> The excellent performance of  $\text{Cu}_{0.3}\text{Ir}_{0.7}\text{O}_\delta$  was confirmed by measuring the Tafel slope to be  $\sim 63 \text{ mV per dec}$  in the acidic solution,  $\sim 203 \text{ mV per dec}$  in the neutral solution and  $\sim 105 \text{ mV per dec}$  in the basic solution. The stability of the prepared  $\text{Cu}_{0.3}\text{Ir}_{0.7}\text{O}_\delta$  was evaluated by conducting chronoamperometry at 1.68 V (vs. RHE) for 6000 s, the results of which are shown in Fig. 1b. In each run, the normalized current slightly decreased due to oxygen bubbles accumulating on the surface, while the CV curves (Fig. 1b insert) before and after 6000 s are almost identical showing that the catalyst remains stable during the OER experiments.

As revealed by nitrogen adsorption isotherms ( $\text{BET m}^2 \text{ g}^{-1}$ ), the prepared catalysts have similar surface areas of 22–30  $\text{m}^2 \text{ g}^{-1}$  (Table S1†). The compositions were characterized by EDS and the spectra are shown in Fig. S1† additional results were listed in Table S2.† Transmission electron microscopy (TEM) showed that Cu-doped  $\text{IrO}_2$  had a short rod-like morphology structure that was different from the  $\text{IrO}_2$  grain morphology (Fig. S2†); this was confirmed by scanning electron microscopy (SEM), as shown in Fig. S3.† It should be noted that the doping

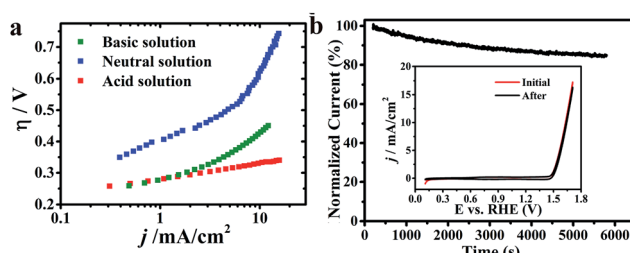


Fig. 1 OER activity of  $\text{Cu}_{0.3}\text{Ir}_{0.7}\text{O}_\delta$  in three solutions of different pH. (a) Tafel curves of  $\text{Cu}_{0.3}\text{Ir}_{0.7}\text{O}_\delta$ . The  $R$  in the three solutions was  $\sim 18 \Omega$  (acid),  $\sim 15 \Omega$  (neutral) and  $\sim 28 \Omega$  (basic), respectively. (b) Chronoamperometric curves at the constant potential 1.68 V vs. RHE. The inset shows the polarization curves for  $\text{Cu}_{0.3}\text{Ir}_{0.7}\text{O}_\delta$  at the initial time point and after the chronoamperometric experiments. The catalyst loadings were  $0.2 \text{ mg cm}^{-2}$  on a Ti plate.

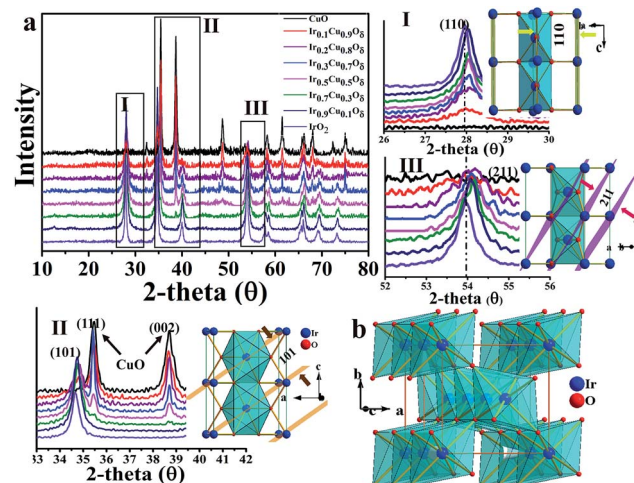


Fig. 2 (a) XRD patterns of the  $\text{Cu}_x\text{Ir}_{1-x}\text{O}_\delta$  compositions with different amounts of Cu doping. (I)–(III) correspond to the (a) selected areas. (b) Polyhedron picture of one  $\text{IrO}_2$  cell.

with Cu could change the  $\text{IrO}_2$  lattice; thus, we have investigated how Cu doping can affect the  $\text{IrO}_2$  rutile structure. The composition was shown to be maintained; its rutile structure at  $x = 0\text{--}0.3$  and, when doped, at  $x > 0.3$ , it was found to be a mixture made up of  $\text{CuO}$  and partially doped  $\text{IrO}_2$ . X-ray diffraction (XRD, Fig. 2a) shows the diffraction planes (002) and (111) corresponding to  $\text{CuO}$ , which peak near  $x = 0.3$ , begin very weakly and increase gradually as more Cu is added, indicating that  $x = 0.3$  is the maximum concentration for solid solution formation. It was also found that Ir could not insert into the  $\text{CuO}$  lattice even at a 10% molar ratio due to the different crystal

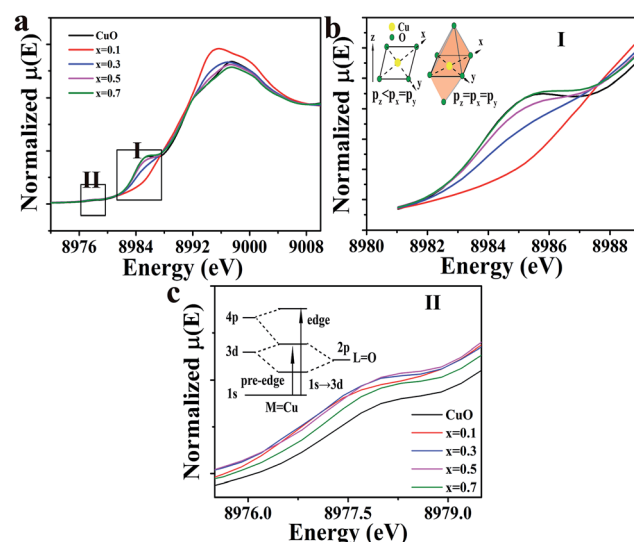


Fig. 3 (a) Normalized Cu-K edge XANES spectra for  $\text{Cu}_x\text{Ir}_{1-x}\text{O}_\delta$  compositions. (b) Shows the shakedown transition and the inset is a diagram of the Cu-4p orbital energy in two different symmetries. (c) Shows the amplified pre-edge region and the inset diagram shows the energy level of possible transitions. (b) and (c) correspond to the selected areas, I and II, in (a).



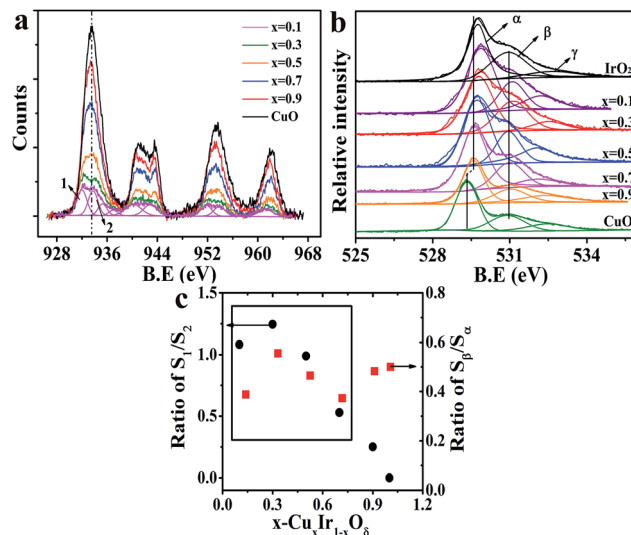


Fig. 4 (a) XPS spectra of Cu-2p in the Cu<sub>x</sub>Ir<sub>1-x</sub>O<sub>δ</sub> compositions with  $x = 0.1$  de-convoluted; other compositions' de-convoluted spectra are shown in the ESI. (b) XPS spectra of O-1s in the Cu<sub>x</sub>Ir<sub>1-x</sub>O<sub>δ</sub> compositions. (c) Pattern of the ratio of  $S_1/S_2$  and  $S_\beta/S_\alpha$  versus the doped amount  $x$ .

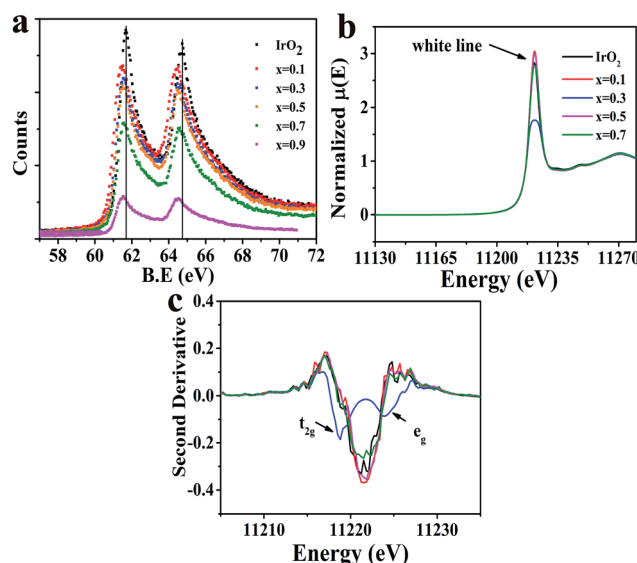


Fig. 5 (a) XPS spectra of Ir-4f in Cu<sub>x</sub>Ir<sub>1-x</sub>O<sub>δ</sub> compositions. The solid vertical lines correspond to the Ir-4f<sub>7/2</sub> and 4f<sub>5/2</sub> peak positions of IrO<sub>2</sub>. (b) Normalized Ir-L<sub>III</sub> edge XANES spectra for Cu<sub>x</sub>Ir<sub>1-x</sub>O<sub>δ</sub> compositions. (c) Second derivatives of Ir-L<sub>III</sub> edge XANES spectra for Cu<sub>x</sub>Ir<sub>1-x</sub>O<sub>δ</sub> compositions.

systems present. It was also confirmed by performing EDX mapping (Fig. S4†) that Cu was homogeneously doped into the IrO<sub>2</sub> lattice with a low Cu composition (for  $x = 0.1$  and  $x = 0.3$ ).

These results were confirmed by the Cu-K edge X-ray absorption near-edge structure (XANES), as shown in Fig. 3a. The Cu-K edge of the CuO separated into two regions in planar symmetry, which were a  $1s \rightarrow 4p_z$  transition, corresponding to the low energy peak (*i.e.*, the shakedown peak), and  $1s \rightarrow 4p_{x,y}$

transitions, corresponding to the primary edge.<sup>36</sup> The local symmetry of Cu, however, had changed to an octahedral symmetry as Cu substituted into Ir sites, and the shakedown peak disappeared due to the isotropic 4p orbital.<sup>36,37</sup> Therefore, no shakedown peak was observed at  $x = 0.1$  and  $0.3$  in the XANES, which was confirmed by the extended X-ray adsorption fine structure (EXAFS) of the Cu-K edge shown in Fig. S5.† However, the intensity of  $x = 0.3$  is shown to be above that of  $x = 0.1$ , which indicated that the octahedron might be distorted. All of the samples studied showed a weak pre-edge peak, which was assigned to  $1s \rightarrow 3d$  due to the quadruple-allowed transition (see Fig. 3a II); this intensity could be achieved by the metal 4p<sub>z</sub> orbital mixing into the 3d orbitals; however, this is not possible due to centrosymmetric complexities.<sup>36-39</sup> A significant feature was also noted: the peak intensity of the doped samples was above that of CuO, indicating the excited distortion of the CuO<sub>6</sub> octahedra at  $x = 0.3$  and  $0.5$ .

As shown, the Cu doping produces an elongated IrO<sub>6</sub> octahedron due to the CuO<sub>6</sub> octahedron's strong Jahn-Teller effect,<sup>40,41</sup> in which the four equatorial oxygen atoms form a plane that compresses, while the apical oxygen out of the plane forms an extended octahedron. The IrO<sub>2</sub> rutile structure exhibits edge sharing along the *c* axis to form chains, and each chain is linked with four neighboring chains by their shared corners (see Fig. 2b). The Ir-O bonds of the IrO<sub>6</sub> octahedra are not equal<sup>42</sup> (4L + 2S) and include four longer Ir-O bonds in plane along with two short ones that correspond to the apical O. As mentioned above, as a result of the Jahn-Teller effect of CuO<sub>6</sub>, the apical O in the CuO<sub>6</sub> octahedron is out of plane, compressing the equatorial O of the neighboring Ir site, and compressed Cu-O bonds of the plane likely make the neighboring apical Ir-O bonds longer. The XRD data of the compounds shows that the shift values of the (110) plane, which describes the *a* axial length, were smaller compared to (101) and (211), which are both represented by *a* and *c* axial lengths. This results in the axial ratio *c/a*, a critical parameter for the rutile structure, being decreased compared to that of IrO<sub>2</sub>. The calculated lattice parameters of all samples are listed in Table S3† based on the XRD data. The results of the performed selected area electron diffraction (SAED) are shown in Fig. S2† and show that the *d*-space of the specified planes decreased after Cu doping. The HRTEM of the samples shown in Fig. S6† also revealed that the *d*-space of the (200) plane was similar between the Cu-doped samples and IrO<sub>2</sub>. The data extracted from the EXAFS spectra (see Fig. S7†) of the Ir-L<sub>III</sub> edge also showed that the Ir-O bond lengths are marginally longer than those of IrO<sub>2</sub> in the samples doped with Cu, while the Ir-Ir peak corresponding to the *c* axis decreased significantly compared to IrO<sub>2</sub>, indicating a reduced *c/a* ratio, which is consistent with the XRD and SAED data discussed above. All of these data indicate that the IrO<sub>2</sub> doped with Cu had a significant lattice distortion with elongated Ir-O bonds for apical O and compressed Ir-O bonds for equatorial O.

It has been shown that oxygen vacancies (Vo)<sup>43,44</sup> will be generated due to the substituted Cu occupying the lattice sites of Ir because the dopant (Cu) charge (+2) is different to the host (Ir) charge (+4); the crystal must maintain its electrical



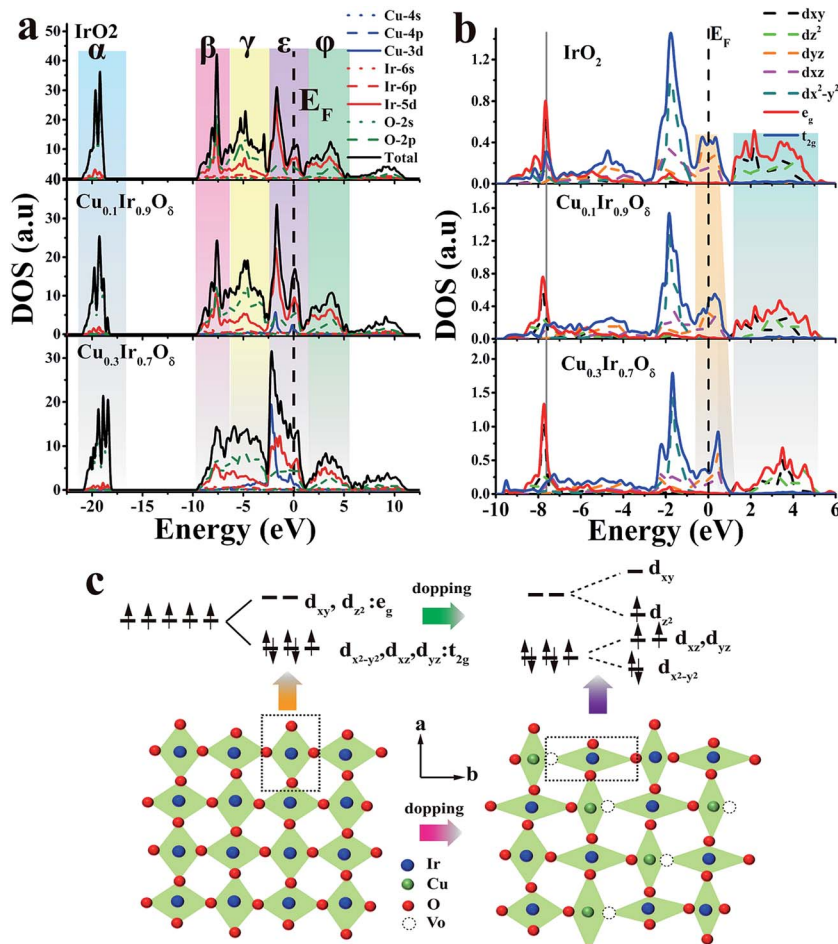


Fig. 6 (a) Densities of states for IrO<sub>2</sub>, Cu<sub>0.1</sub>Ir<sub>0.9</sub>O<sub>δ</sub> and Cu<sub>0.3</sub>Ir<sub>0.7</sub>O<sub>δ</sub>. The colored regions are marked by Greek letters. (b) Partial densities of states for IrO<sub>2</sub>, Cu<sub>0.1</sub>Ir<sub>0.9</sub>O<sub>δ</sub> and Cu<sub>0.3</sub>Ir<sub>0.7</sub>O<sub>δ</sub>. (c) Schematic lattice diagram in the ab plane of IrO<sub>2</sub> (left) and substituted by Cu (right). The top row shows Ir-5d orbital degeneracy of IrO<sub>2</sub> (left) and the lift degeneracy and electron redistribution by doping with Cu.

neutrality to retain no net charge in the crystal structure; this produces a vacancy. These vacancies are identified and labeled as  $\beta$  in the O-1s core level spectrum shown in Fig. 4b. Fig. 4a shows the Cu-2p core level spectrum of the doped materials and that of CuO for reference (detail in Fig. S8†). It is clearly noted that two de-convoluted peaks were identified and labeled as 1 and 2 at 2p<sub>3/2</sub> in the doped material at  $x = 0.1$  and 0.3; this finding indicated that two different states of the doped Cu corresponded to high and low valence states, respectively. The binding energy of peak 2 was marginally above that of the CuO sample, perhaps corresponding to the O-Cu-O-Ir-O situation. The electronegativity of Cu (*i.e.*, the Pauling electronegativity is 1.9) is below that of Ir (*i.e.*, the Pauling electronegativity is 2.2), meaning that oxygen is more inclined to gain an electron from copper. This was also confirmed by the O-1s XPS spectra; the primary peak labeled  $\alpha$  originated from the metal (Cu, Ir)-O bond in the lattice, and the binding energy progressively decreased with the increasing Cu concentration. The ratio of S<sub>1</sub>/S<sub>2</sub> and S<sub>β</sub>/S<sub>α</sub> (*i.e.*, S-peak area) *versus* the doped amount  $x$  is shown in Fig. 4c. It was noted that the variation of S<sub>1</sub>/S<sub>2</sub> and S<sub>β</sub>/S<sub>α</sub> in Cu<sub>x</sub>Ir<sub>1-x</sub>O<sub>δ</sub> showed a similar tendency as the doping amount increased but remained below  $x \leq 0.7$ ; this indicated

that there was a strong relationship between the low valence state of the doped Cu and that of the Vo. Thus, we inferred that the oxygen defects were generally closer to the Cu sites. As discussed above, the *c*-axis of a unit cell with doped Cu was reduced and was directly related to the planar oxygen in the octahedron. Thus, we inferred that the lattice oxygen defects might occur in the plane of the CuO<sub>6</sub> octahedron rather than at the apical location and that the defect position corresponded to the apical O of the IrO<sub>6</sub> octahedron.

This study then investigated how the modified IrO<sub>2</sub> doped by Cu affects the electronic structure of the Ir site. As shown in Fig. 5a (Ir-4f XPS), a shift to a lower binding energy was clearly observed in the doped samples compared to IrO<sub>2</sub>, suggesting a higher electron density at the Ir site. We thus did not assign a low valence to Ir in all samples (see discussion in Fig. S9†). The performed Ir-L<sub>III</sub> edge XANES (Fig. 5b) revealed that an increasing number of Ir-5d states were occupied with IrO<sub>2</sub> doped at  $x = 0.3$  with Cu due to a significant decrease in intensity in the so-called “white line region”. The edge positions of the Ir-L<sub>III</sub> edge for all of the prepared materials were found to be similar, indicating no valence change on Ir. In the ionic model, the five 5d electrons of the Ir<sup>4+</sup> ion in IrO<sub>2</sub> were shown to



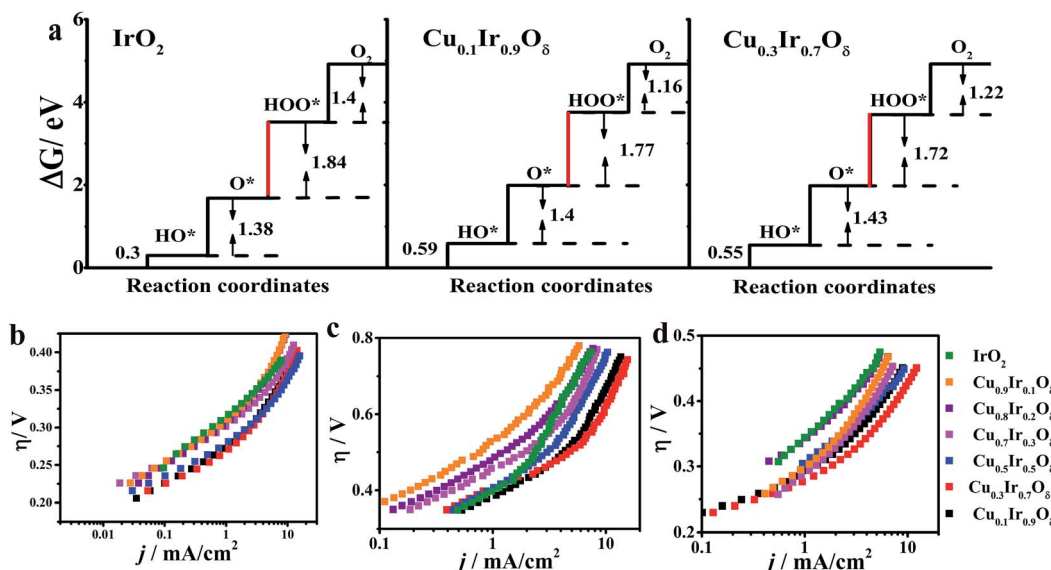


Fig. 7 (a) Standard free energy diagram for the OER in IrO<sub>2</sub>, Cu<sub>0.1</sub>Ir<sub>0.9</sub>O<sub>δ</sub> and Cu<sub>0.3</sub>Ir<sub>0.7</sub>O<sub>δ</sub>. (b–d) Tafel plots in acidic, neutral and basic solutions, respectively. The curves are iR-corrected in the acidic (~18 Ω), neutral (~15 Ω) and basic (~28 Ω) solutions, respectively. The catalyst mass loading was ~0.2 mg cm<sup>−2</sup> for all electrodes.

occupy the t<sub>2g</sub> triplet (*i.e.*, d<sub>xz</sub>, d<sub>yz</sub> and d<sub>x<sup>2</sup>-y<sup>2</sup></sub>) and leave the higher e<sub>g</sub> doublet (*i.e.*, d<sub>xy</sub> and d<sub>z<sup>2</sup></sub>) empty under the octahedral crystal field described by the t<sub>2g</sub><sup>5</sup>e<sub>g</sub><sup>0</sup> configuration.<sup>45,46</sup> However, as shown in the second derivative spectra (Fig. 5c), only a single feature was observed for IrO<sub>2</sub> due to the IrO<sub>6</sub> octahedron being cross-linked to form a 3D structure; this can be explained by a bond model.<sup>47,48</sup> In contrast, the doublet feature was found in some iridate perovskite compositions with the IrO<sub>6</sub> octahedron being regarded as a single cluster. Therefore, Fig. 5c confirms that x = 0.3 produces a doublet in the white line structure, and other doped compositions yielded results similar to that of IrO<sub>2</sub>. One of surprising features at x = 0.3 was that the peak intensity and area of the 2p → t<sub>2g</sub> (5d) transition were increased above those of the 2p → e<sub>g</sub> (5d) transition, which are in contrast to the findings in iridate perovskites,<sup>47,48</sup> thus, we inferred that the e<sub>g</sub> state had been partially occupied.

The Cu doping led to an IrO<sub>2</sub> lattice distortion due to the CuO<sub>6</sub> octahedron's Jahn-Teller effect and also generated oxygen defects, which significantly affected the energy distribution of the d-orbitals of Ir sites. The density of states (DOS) is a good descriptor for the bonding character and occupancy of the orbital states.<sup>49–52</sup> Fig. 6a and b showed the DOS of IrO<sub>2</sub> and the doped material at x = 0.1 and 0.3 using the general gradient approximation (GGA) calculation; details of this analysis are shown in the calculation section of the ESI.† The colored region of Fig. 6a labels α, β, γ, ε and φ for Ir–O a<sub>1g</sub> bonding, σ bonding, π bonding, π antibonding (including the non-bonding part) and σ antibonding, respectively.<sup>46,53,54</sup> One of the features of DOS is that the σ and π bonding region changed from narrow to relatively broad, and its antibonding states were pulled to a lower energy level as the Cu doping increased, weakening the bonding; this was primarily due to the occupancy of σ states. The partial DOS (PDOS) of Ir is shown in Fig. 6b. The d<sub>xy</sub> orbital occupied states were located at lower energies (gray solid line),

while the antibonding states moved to higher energies (light blue region) as the Cu doping amount increased, indicating that the d<sub>xy</sub> orbital was uplifted. In contrast, the d<sub>z<sup>2</sup></sub> antibonding states were shifted to a lower energy level. The d<sub>xz</sub> and d<sub>yz</sub> bands were crossed by the Fermi level (E<sub>F</sub>), which changed to a narrow shape and was pushed above E<sub>F</sub>, indicating that the bands were empty in the π antibonding orbital; this indicated that the electrons may be half-filled in the d<sub>xz</sub> and d<sub>yz</sub> orbital. The d<sub>x<sup>2</sup>-y<sup>2</sup></sub> band showed nearly no variation when fully occupied, even when doped with Cu. As discussed above, the Ir-5d electrons showed lifted degeneracy in the octahedron within Cu; this made the d<sub>z<sup>2</sup></sub> orbital energy decrease, while the d<sub>xy</sub> orbital energy increased. As a result, an electron might hop to the d<sub>z<sup>2</sup></sub> orbital (see Fig. 6c), making the e<sub>g</sub> orbital partially filled.

Based on the density functional theory (DFT) and the molecular orbital principles, a strong or weak bond formation from a surface site interacting with the reaction intermediates is strongly correlated with the OER activity. A σ bond to a e<sub>g</sub> orbital facilitates bonding with oxygen intermediates compared to a π bond t<sub>2g</sub> orbital due to the e<sub>g</sub> orbital's stronger overlap with O-2p.<sup>8,52,55</sup> Suntivich *et al.*<sup>55</sup> proposed that e<sub>g</sub> occupation close to unity optimizes the rate-determining step (RDS) and thereby leads to a higher OER activity and is successful in perovskite studies. Vojvodic and Nørskov<sup>52</sup> showed that the surface-oxygen bond energy correlates with e<sub>g</sub> and t<sub>2g</sub> occupation and has a similar relationship to the interaction between the surface site and O-adsorbate, which becomes weaker with an increasing number of occupied states (*e.g.*, e<sub>g</sub> and t<sub>2g</sub>). The possible OER mechanism on the metal oxides is shown in Fig. S10.† The binding free energies of all the reaction intermediates (HO\*, O\*, HOO\*) involved in Fig. S9† are described in Fig. 7a. For a wide class of metal oxides, a linear relationship was found in the binding free energy between OH\* and O\* equated with  $\Delta G_2 + \Delta G_3 = 3.2 \pm 0.2$  eV.<sup>50,56</sup> As a result, the catalysts have been

optimized, evidenced by the reduction in the difference between  $\Delta G_2$  and  $\Delta G_3$ . It was found that the sum of  $\Delta G_2$  and  $\Delta G_3$  met this relationship for  $\text{IrO}_2$  (3.22 eV),  $\text{Ir}_{0.9}\text{Cu}_{0.1}\text{O}_\delta$  (3.17 eV) and  $\text{Ir}_{0.7}\text{Cu}_{0.3}\text{O}_\delta$  (3.15 eV). In the case of  $\text{IrO}_2$  ( $t_{2g}^5 e_g^0$ ), partial  $e_g$  filling on the Ir sites may result in the electrons of the O-2p adsorbate being able to easily hop to the unoccupied  $\sigma^*$  orbital to form Ir-OH and Ir-O bonds, which decrease the free energies of the first and second step ( $\text{OH}^*$  and  $\text{O}^*$ ). However, the formation of  $\text{OOH}^*$  will occur at the RDS ( $\Delta G_3 = 1.84$  eV) due to the rupture of the surface-oxygen bonds in most of the metal-oxide catalysts. For  $\text{IrO}_2$  doped with Cu ( $x = 0.1$  and  $0.3$ ) with  $e_g$  partially filled on the Ir site, it should take a higher energy to form Ir-OH and Ir-O bonds ( $\Delta G_1 + \Delta G_2 = 1.99$  and  $1.98$  eV higher  $1.68$  eV of  $\text{IrO}_2$ ); however, the difference between  $\Delta G_2$  and  $\Delta G_3$  was found to be decreased ( $\Delta G_3 - \Delta G_2 = 0.37$  eV and  $0.29$  eV comparable to  $0.46$  eV of  $\text{IrO}_2$ ) and reached a lower theoretical overpotential ( $\eta_{\text{the}}(x = 0.3) = 0.39$  eV with  $\eta_{\text{the}}(x = 0) = 0.51$  eV). The experimental data of OER for the studied samples are shown in Fig. 7b-d, which show that, except for  $\text{Cu}_{0.3}\text{Ir}_{0.7}\text{O}_\delta$ , all doped materials exhibited some OER activity; the  $\text{Cu}_{0.2}\text{Ir}_{0.8}\text{O}_\delta$  and  $\text{Cu}_{0.1}\text{Ir}_{0.9}\text{O}_\delta$  compositions had a higher  $j$  compared to  $\text{IrO}_2$  in the basic solutions. In addition, the mechanical mixtures of  $\text{IrO}_2$  and  $\text{CuO}$  were prepared; however, no improvement in OER activity (see Fig. S11†) through mechanical mixing was observed. The  $\eta$  at  $j = 10 \text{ mA cm}^{-2}$ , the Tafel slopes and the mass activities at specific overpotentials in all of the prepared materials are shown in Table S4.† From this table, we can conclude that the Cu doping did enhance the OER activity, and  $x = 0.3$  showed an excellent performance, which was consistent with the results from the relevant physical characterisations and DFT calculations.

## Conclusions

The relevant experimental and theoretical results clearly showed that the d orbital occupation states of  $\text{Ir-5d}$  ( $t_{2g}^5 e_g^0$ ) in  $\text{IrO}_2$  can be tuned by substituting Ir for Cu to create a  $d_z^2$ -anti-bonding orbital (*i.e.*, one of  $e_g$ -antibonding orbitals) that is partially occupied in the  $\text{Cu}_{0.3}\text{Ir}_{0.7}\text{O}_\delta$  composition. The  $\text{Cu}_{0.3}\text{Ir}_{0.7}\text{O}_\delta$  composition exhibited an unexpected OER activity from its Tafel slope to its mass activity in three different pH solutions compared to  $\text{IrO}_2$ . The substitution with Cu into the rutile structure of  $\text{IrO}_2$  inherently had a strong Jahn-Teller effect due to the  $\text{CuO}_6$  octahedron and induced partial oxygen defects in the lattice that changed the  $\text{IrO}_6$  octahedral geometric structure and also lifted degeneracy of the  $t_{2g}$  and  $e_g$  orbitals. Therefore, the proposed method of doping with foreign elements to tune the electron occupation between the  $t_{2g}$  and  $e_g$  orbital states of Ir sites can yield an opportunity to design effective OER catalysts using TMO group materials.

## Acknowledgements

This research is based on work supported by the National Natural Science Foundation of China (21177037, 21277045, 21322307), the Public welfare project of the Ministry of Environmental Protection (201309021), the "Shu Guang" project of

the Shanghai Municipal Education Commission and the Shanghai Education Development Foundation, and the Fundamental Research Funds for the Central Universities. We would like to thank beamline BL14W1 (Shanghai Synchrotron Radiation Facility) for providing the beam time.

## Notes and references

- 1 N. S. Lewis and D. G. Nocera, *Proc. Natl. Acad. Sci. U. S. A.*, 2006, **103**, 15729–15735.
- 2 H. B. Gray, *Nat. Chem.*, 2009, **1**, 7.
- 3 M. G. Walter, E. L. Warren, J. R. McKone, S. W. Boettcher, Q. Mi, E. A. Santori and N. S. Lewis, *Chem. Rev.*, 2010, **110**, 6446–6473.
- 4 J. Chakhalian, A. J. Millis and J. Rondinelli, *Nat. Mater.*, 2012, **11**, 92–94.
- 5 R. I. Cukier and D. G. Nocera, *Annu. Rev. Phys. Chem.*, 1998, **49**, 337–369.
- 6 S. Hammes-Schiffer, *Acc. Chem. Res.*, 2009, **42**, 1881–1889.
- 7 S.-W. Cheong, *Nat. Mater.*, 2007, **6**, 927–928.
- 8 J. Suntivich, H. A. Gasteiger, N. Yabuuchi, H. Nakanishi, J. B. Goodenough and Y. Shao-Horn, *Nat. Chem.*, 2011, **3**, 546–550.
- 9 D. W. Jeong, W. S. Choi, S. Okamoto, J.-Y. Kim, K. W. Kim, S. J. Moon, D.-Y. Cho, H. N. Lee and T. W. Noh, *Sci. Rep.*, 2014, **4**, 6124–6128.
- 10 J. Chakhalian, J. W. Freeland, H.-U. Habermeier, G. Cristiani, G. Khaliullin, M. van Veenendaal and B. Keimer, *Science*, 2007, **318**, 1114–1117.
- 11 Y. Tokura and N. Nagaosa, *Science*, 2000, **288**, 462–468.
- 12 J. K. Norskov, T. Bligaard, J. Rossmeisl and C. H. Christensen, *Nat. Chem.*, 2009, **1**, 37–46.
- 13 C. A. Kent, J. J. Concepcion, C. J. Dares, D. A. Torelli, A. J. Rieth, A. S. Miller, P. G. Hoertz and T. J. Meyer, *J. Am. Chem. Soc.*, 2013, **135**, 8432–8435.
- 14 P. Liao, J. A. Keith and E. A. Carter, *J. Am. Chem. Soc.*, 2012, **134**, 13296–13309.
- 15 J. Park, H. Kim, K. Jin, B. J. Lee, Y.-S. Park, H. Kim, I. Park, K. D. Yang, H.-Y. Jeong, J. Kim, K. T. Hong, H. W. Jang, K. Kang and K. T. Nam, *J. Am. Chem. Soc.*, 2014, **136**, 4201–4211.
- 16 B. S. Yeo and A. T. Bell, *J. Am. Chem. Soc.*, 2011, **133**, 5587–5593.
- 17 Q. Zhang, Z. D. Wei, C. Liu, X. Liu, X. Q. Qi, S. G. Chen, W. Ding, Y. Ma, F. Shi and Y. M. Zhou, *Int. J. Hydrogen Energy*, 2012, **37**, 822–830.
- 18 D. M. Jang, I. H. Kwak, E. L. Kwon, C. S. Jung, H. S. Im, K. Park and J. Park, *J. Phys. Chem. C*, 2015, **119**, 1921–1927.
- 19 K. S. Kadakia, P. H. Jampani, O. I. Velikokhatnyi, M. K. Datta, S. K. Park, D. H. Hong, S. J. Chung and P. N. Kumta, *J. Power Sources*, 2014, **269**, 855–865.
- 20 S. Siracusano, N. Van Dijk, E. Payne-Johnson, V. Baglio and A. S. Aricò, *Appl. Catal., B*, 2015, **164**, 488–495.
- 21 J. Cheng, H. Zhang, G. Chen and Y. Zhang, *Electrochim. Acta*, 2009, **54**, 6250–6256.
- 22 C. Felix, T. Maiyalagan, S. Pasupathi, B. J. Bladergroen and V. Linkov, *Int. J. Electrochem. Sci.*, 2012, **7**, 12064–12077.

23 E. Kuznetsova, V. Petrykin, S. Sunde and P. Krtík, *Electrocatalysis*, 2015, **6**, 198–210.

24 C. De Pauli and S. Trasatti, *J. Electroanal. Chem.*, 2002, **538**, 145–151.

25 M. Yagi, E. Tomita, S. Sakita, T. Kuwabara and K. Nagai, *J. Phys. Chem. B*, 2005, **109**, 21489–21491.

26 Y. Lee, J. Suntivich, K. J. May, E. E. Perry and Y. Shao-Horn, *J. Phys. Chem. Lett.*, 2012, **3**, 399–404.

27 Y. Zhao, E. A. Hernandez-Pagan, N. M. Vargas-Barbosa, J. L. Dysart and T. E. Mallouk, *J. Phys. Chem. Lett.*, 2011, **2**, 402–406.

28 J. Ghijsen, L. H. Tjeng, J. van Elp, H. Eskes, J. Westerink, G. A. Sawatzky and M. T. Czyzyk, *Phys. Rev. B*, 1988, **38**, 11322–11330.

29 R. Fehrenbacher and T. M. Rice, *Phys. Rev. Lett.*, 1993, **70**, 3471–3474.

30 C. Varma, P. B. Littlewood, S. Schmitt-Rink, E. Abrahams and A. Ruckenstein, *Phys. Rev. Lett.*, 1989, **63**, 1996.

31 A. Minguzzi, F.-R. F. Fan, A. Vertova, S. Rondinini and A. J. Bard, *Chem. Sci.*, 2012, **3**, 217–229.

32 Y. Gorlin and T. F. Jaramillo, *J. Am. Chem. Soc.*, 2010, **132**, 13612–13614.

33 M.-R. Gao, X. Cao, Q. Gao, Y.-F. Xu, Y.-R. Zheng, J. Jiang and S.-H. Yu, *ACS Nano*, 2014, **8**, 3970–3978.

34 M.-R. Gao, Y.-F. Xu, J. Jiang, Y.-R. Zheng and S.-H. Yu, *J. Am. Chem. Soc.*, 2012, **134**, 2930–2933.

35 Y. Liang, Y. Li, H. Wang, J. Zhou, J. Wang, T. Regier and H. Dai, *Nat. Mater.*, 2011, **10**, 780–786.

36 J.-H. Choy, D.-K. Kim, S.-H. Hwang and G. Demazeau, *Phys. Rev. B*, 1994, **50**, 16631–16639.

37 L. S. Kau, D. J. Spira-Solomon, J. E. Penner-Hahn, K. O. Hodgson and E. I. Solomon, *J. Am. Chem. Soc.*, 1987, **109**, 6433–6442.

38 J. L. DuBois, P. Mukherjee, A. M. Collier, J. M. Mayer, E. I. Solomon, B. Hedman, T. D. P. Stack and K. O. Hodgson, *J. Am. Chem. Soc.*, 1997, **119**, 8578–8579.

39 J. L. DuBois, P. Mukherjee, T. D. P. Stack, B. Hedman, E. I. Solomon and K. O. Hodgson, *J. Am. Chem. Soc.*, 2000, **122**, 5775–5787.

40 G.-M. Zhao, M. B. Hunt, H. Keller and K. A. Muller, *Nature*, 1997, **385**, 236–239.

41 G. Peralta, D. Puggioni, A. Filippetti and V. Fiorentini, *Phys. Rev. B*, 2009, **80**, 140408.

42 A. A. Bolzan, C. Fong, B. J. Kennedy and C. J. Howard, *Acta Crystallogr., Sect. B*, 1997, **53**, 373–380.

43 J. Wang, Z. Wang, B. Huang, Y. Ma, Y. Liu, X. Qin, X. Zhang and Y. Dai, *ACS Appl. Mater. Interfaces*, 2012, **4**, 4024–4030.

44 J. Gan, X. Lu, J. Wu, S. Xie, T. Zhai, M. Yu, Z. Zhang, Y. Mao, S. C. I. Wang, Y. Shen and Y. Tong, *Sci. Rep.*, 2013, **3**, 1021–1027.

45 Y. Hirata, K. Ohgushi, J.-I. Yamaura, H. Ohsumi, S. Takeshita, M. Takata and T.-H. Arima, *Phys. Rev. B*, 2013, **87**, 161111.

46 J. Kahk, C. Poll, F. Oropesa, J. Ablett, D. Céolin, J. Rueff, S. Agrestini, Y. Utsumi, K. Tsuei and Y. Liao, *Phys. Rev. Lett.*, 2014, **112**, 117601.

47 J.-H. Choy, D.-K. Kim, G. Demazeau and D.-Y. Jung, *J. Phys. Chem.*, 1994, **98**, 6258–6262.

48 J.-H. Choy, D.-K. Kim, S.-H. Hwang, G. Demazeau and D.-Y. Jung, *J. Am. Chem. Soc.*, 1995, **117**, 8557–8566.

49 B. Hammer and J. K. Nørskov, in *Advances in Catalysis*, ed. C. Bruce and H. K. Gates, Academic Press, 2000, vol. 45, pp. 71–129.

50 I. C. Man, H. Y. Su, F. Calle-Vallejo, H. A. Hansen, J. I. Martínez, N. G. Inoglu, J. Kitchin, T. F. Jaramillo, J. K. Nørskov and J. Rossmeisl, *ChemCatChem*, 2011, **3**, 1159–1165.

51 J. Rossmeisl, Z.-W. Qu, H. Zhu, G.-J. Kroes and J. K. Nørskov, *J. Electroanal. Chem.*, 2007, **607**, 83–89.

52 A. Vojvodic and J. K. Nørskov, *Science*, 2011, **334**, 1355–1356.

53 J. S. de Almeida and R. Ahuja, *Phys. Rev. B*, 2006, **73**, 165102.

54 L. F. Mattheiss, *Phys. Rev. B*, 1976, **13**, 2433–2450.

55 J. Suntivich, K. J. May, H. A. Gasteiger, J. B. Goodenough and Y. Shao-Horn, *Science*, 2011, **334**, 1383–1385.

56 S. Piccinin, A. Sartorel, G. Aquilanti, A. Goldoni, M. Bonchio and S. Fabris, *Proc. Natl. Acad. Sci. U. S. A.*, 2013, **110**, 4917–4922.

